Exploration of oxyfluoride frameworks as Na-ion cathodes

Debolina Deb[1] and Gopalakrishnan Sai Gautam[1,*]

[1]Department of Materials Engineering, Indian Institute of Science, Bengaluru, 560012, India

*Email: saigautamg@iisc.ac.in

Abstract

Na-ion batteries (NIBs) are increasingly looked at as a viable alternative to Li-ion batteries due to the abundance, low cost, and thermal stability of Na-based systems. To improve the practical utilization of NIBs in applications, it is important to boost the energy and power densities of the electrodes being used, via discovery of novel candidate materials. Thus, we explore the chemical space of transition metal containing oxyfluorides (TMOFs) that adopt the perovskite structure as possible NIB electrodes. Our choice of the perovskite structure is motivated by the 'large' cationic tunnels that can accommodate Na^+, while the chemistry of TMOFs is motivated by the high electronegativity and inductive effect of F^-, which can possibly lead to higher voltages. We use density functional theory based calculations to estimate the ground state polymorphs, average Na (de)intercalation voltages, thermodynamic stabilities and Na^+ mobility on two distinct sets of compositions: the F-rich Na_xMOF_2, and the O-rich $Na_{1+x}MO_2F$ where $x = 0$–1 and M = Ti, V, Cr, Mn, Fe, Co, or Ni. Upon identifying the ground state polymorphs in the charged compositions (i.e., MOF_2 and $NaMO_2F$), we show that F-rich perovskites exhibit higher average voltages compared to O-rich perovskites. Also, we find six stable/metastable perovskites in the F-rich space, while all O-rich perovskites (except $NaTiO_2F$) are unstable. Finally, our Na-ion mobility calculations indicate that $TiOF_2$-$NaTiOF_2$, VOF_2-$NaVOF_2$, $CrOF_2$, and $NaMnOF_2$ can be promising compositions for experimental exploration as NIB cathodes, primarily if used in a strained electrode configuration and/or thin film batteries. Our computational approach and findings provide insights into developing practical NIBs involving fluorine-containing intercalation frameworks.

1 Introduction

Na-ion battery (NIB) technology is a key contributor in reducing the extensive dependence on Li-ion batteries (LIBs) to fulfil the ever-increasing energy demands. [1–5] As a technology, NIBs have come a long way with notable applications in both electric vehicles and stationary energy storage. [6–9] Nevertheless, the practical utility of NIBs can be further enhanced with the development of novel high energy and power density electrode materials. While layered transition-metal oxides (TMOs) are the state-of-the-art NIB positive electrodes (cathodes), [10] the structural instabilities of layered compounds at their fully desodiated states and detrimental phase transitions have directed research towards polyanionic cathode frameworks. [11–13] Some of the most explored polyanionic frameworks, such as the sodium superionic conductors (NaSICONs), alluaudites, olivines, and pyro/fluoro-phosphates display a wide range of electrochemical performance and good structural stability, with low gravimetric capacity being a common impediment. [12] Thus, an ideal NIB

cathode must be able to (de)intercalate the large Na$^+$ at high rates, without compromising on structural stability, and deliver a large capacity for achieving both high energy and power densities. An ideal NIB negative electrode (anode) has similar requirements as the ideal cathode as well.

Oxide perovskites, which have a general formula of ABO$_3$, where A and B are cations, have been explored for several non-energy-storage applications, due to their structural stability and compositional flexibility. [14–18] Importantly, perovskites are suitable structures for accommodating Na$^+$ because of their rigid open structures with large voids. [19] Additionally, incorporation of fluorides in cathode frameworks often leads to improved energy densities, since the higher electronegativity of F$^-$ typically leads to a higher (de)intercalation voltage via the induction effect. [20–22] Indeed, many of the best-performing polyanionic NIB cathodes contain fluorine. [23–25] Thus, fixing the A cation in a perovskite as Na$^+$, the B cation to be a redox-active 3d transition metal (TM), and the anions being a mixture of both O and F, yields a class of perovskite-based TM oxyflouride (TMOFs) compositions as potential NIB cathodes (or anodes).

So far, perovskite TMOFs are a largely unexplored class of battery cathodes (or anodes), primarily due to synthesis difficulties from highly stable fluoride precursors. [26] Indeed, only a few TMOFs, including, TiOF$_2$ (space group: $Pm\bar{3}m$), [27] VO$_2$F ($R\bar{3}c$), [28, 29] and NbO$_2$F ($Pm\bar{3}m$), [27] have been investigated as LIB cathodes. Additionally, Li$_2$MO$_2$F with M across the 3d series [30] and Na$_2$MnO$_2$F [31] have been reported to exhibit a disordered rocksalt, and not a perovskite-based structure. Also, most of the oxyfluoride structures that have been reported have undergone either amorphization or an irreversible structural transition during electrochemical cycling. [32–35] Although Li-ion mobility is not hindered in both disordered rocksalt, [36] and amorphized, [37] oxyfluorides, studies have not analysed Na-ion mobility in similar frameworks. Notably, the rutile-FeOF ($P4_2/mnm$) structure was tested as a NIB cathode and showed a reversible transition to cubic-Na$_x$FeOF. [35] However, this FeOF↔Na$_x$FeOF transition was accompanied by significant hysteresis in the corresponding voltage-capacity profiles, with possible contributions from electrolyte decomposition and/or other side reactions. [35] Importantly, the chemical class TMOFs has not been systematically explored, either computationally or experimentally, as NIB cathodes, so far.

Here, we present a systematic density functional theory (DFT)-based computational exploration of perovskite-based TMOF compositions as potential NIB cathodes (or anodes). Specifically, we explore the chemical compositions of oxygen-rich (NaMO$_2$F↔Na$_2$MO$_2$F) and fluorine-rich (MOF$_2$ ↔NaMOF$_2$) perovskites, where M = Ti, V, Cr, Mn, Fe, Co, or Ni. For both O-rich and F-rich compositions, we examine possible crystalline structures of the general perovskite framework. Importantly, we have evaluated the ground state Na-vacancy configurations, average Na intercalation voltages, and the 0 K thermodynamic stabilities in both O-rich and F-rich TMOFs, followed by an evaluation of the Na-ion mobility in a subset of candidate compounds. Besides shedding light on the overall trends in voltages and stabilities, we also identify a few promising compositions, namely, TiOF$_2$-NaTiOF$_2$, VOF$_2$-NaVOF$_2$, CrOF$_2$ and NaMnOF$_2$, as candidate NIB electrodes which can be relevant for subsequent experimental validation, primarily in strained configurations. We hope that our study opens up the novel oxyfluoride chemical space for battery cathode applications and beyond.

2

2 Methods and Workflow

2.1 Structure identification

To explore the TMOF chemical space, we used the charged O-rich (i.e., $NaMO_2F$) and F-rich (MOF_2) compositions as the initial cases for structure generation for all TMs. Note that both the charged compositions correspond to the TM being in a +4 oxidation state, while the corresponding discharged compositions (Na_2MO_2F and $NaMOF_2$) reflect the TM in a +3 oxidation state. To identify the relevant space group/polymorph, we first searched the inorganic crystal structure database (ICSD [38]) for experimental structures with the $NaMO_2F$ and MOF_2 compositions, where we found only $TiOF_2$ (ICSD collection code 160661; $Pm\bar{3}m$), VO_2F (ICSD collection code 142594; $R\bar{3}c$) and $LiVO_2F$ (ICSD collection code 142596; $R\bar{3}c$). Thus, we used the $TiOF_2$ structure from the ICSD as the starting configuration for all calculations involving cubic-$TiOF_2$, VO_2F for calculations of rhombohedral-MOF_2, and $LiVO_2F$ for calculations of rhombohedral-$NaMO_2F$.

Given the absence of ICSD structures for other TMOFs, we theoretically generated possible structures for both charged compositions, using the workflow displayed in **Figure 1**. Similar to the procedure used in a previous study [18], we used experimental template structures among six different space groups that are commonly adopted by perovskite compositions to generate six possible theoretical structures for each composition. Specifically, we used $CaTiO_3$, $BaTiO_3$, $NaNbO_2F$, $BaRhO_3$, $LiVO_2F$, and $CeVO_3$ as templates for the $Pm\bar{3}m$, $P4mm$, $Pbnm$, $P63/mmc$, $R\bar{3}c$, and $P2/b$ space groups, respectively. We chose Ba and Ca containing structures as templates due to the similarity in ionic radii of Ba^{2+} and Ca^{2+} to Na^+. $CeVO_3$ was the only reasonable monoclinically-distorted perovskite template we could find. For rhombohedral perovskites, the presence of VO_2F and $LiVO_2F$ experimental structures provided us both an oxyfluoride template along with possible Na sites, as Li can be substituted with Na, [39] motivating our use of $LiVO_2F$ as the template. [28] As far the orthorhombic perovskite, $NaNbO_2F$ is an oxyfluoride and contains Na, and hence was the obvious choice as a template. Note that we used the $TiOF_2$ structure as the $Pm\bar{3}m$ template for other MOF_2 compositions, while we used the $CaTiO_3$ structure as the $Pm\bar{3}m$ template for $NaMO_2F$ compositions. In addition, we used VO_2F structure as the $R\bar{3}c$ template for all rhombohedral-MOF_2 compositions and $LiVO_2F$ structure as the $R\bar{3}c$ template for all rhombohedral-$NaMO_2F$ compositions.

From each template structure, we performed chemical substitution (i.e., replace Ca/Ba/Li/Ce with Na, and the remaining cation with a $3d$ TM), to result in a $NaMO_3$ composition. Subsequenty, we used the RLSVolumePredictor [40] class of the pymatgen package to scale the lattice parameters of the template structure to values that better represent a $NaMO_3$ perovskite composition. Upon lattice scaling, we introduced F, based on a O:F ratio of 2:1 in O-rich perovskites, and 1:2 in F-rich perovskites, by inducing disorder within the anionic sublattice using the SubstitutionTransformation class of pymatgen. Note that in F-rich perovskites, we removed the Na before the lattice scaling step. Finally, we enumerated symmetrically distinct O-F arrangements for all distinct template space groups in both the $NaMO_2F$ and MOF_2 compositions, using the OrderDisorderedStructureTransformation class of pymatgen, and performed DFT calculations to determine the respective ground state configurations. During enumerations, we took a maximum of 16 structures that exhibited the lowest electrostatic energy, calculated using the Ewald summation technique, [41] to minimize computational expense. In the case of $P4mm$ and $R\bar{3}c$ perovskites (both MOF_2 and $NaMOF_2$), we obtained a total of only five and three symmetrically distinct configurations upon enumeration and all configurations were considered for DFT calculations. In the case of $Pm\bar{3}m$, $Pbnm$, $P63/mmc$, and $P2/b$ space groups, we obtained a total of 22, 40, 55, and 48 symmetrically distinct configurations, respectively,
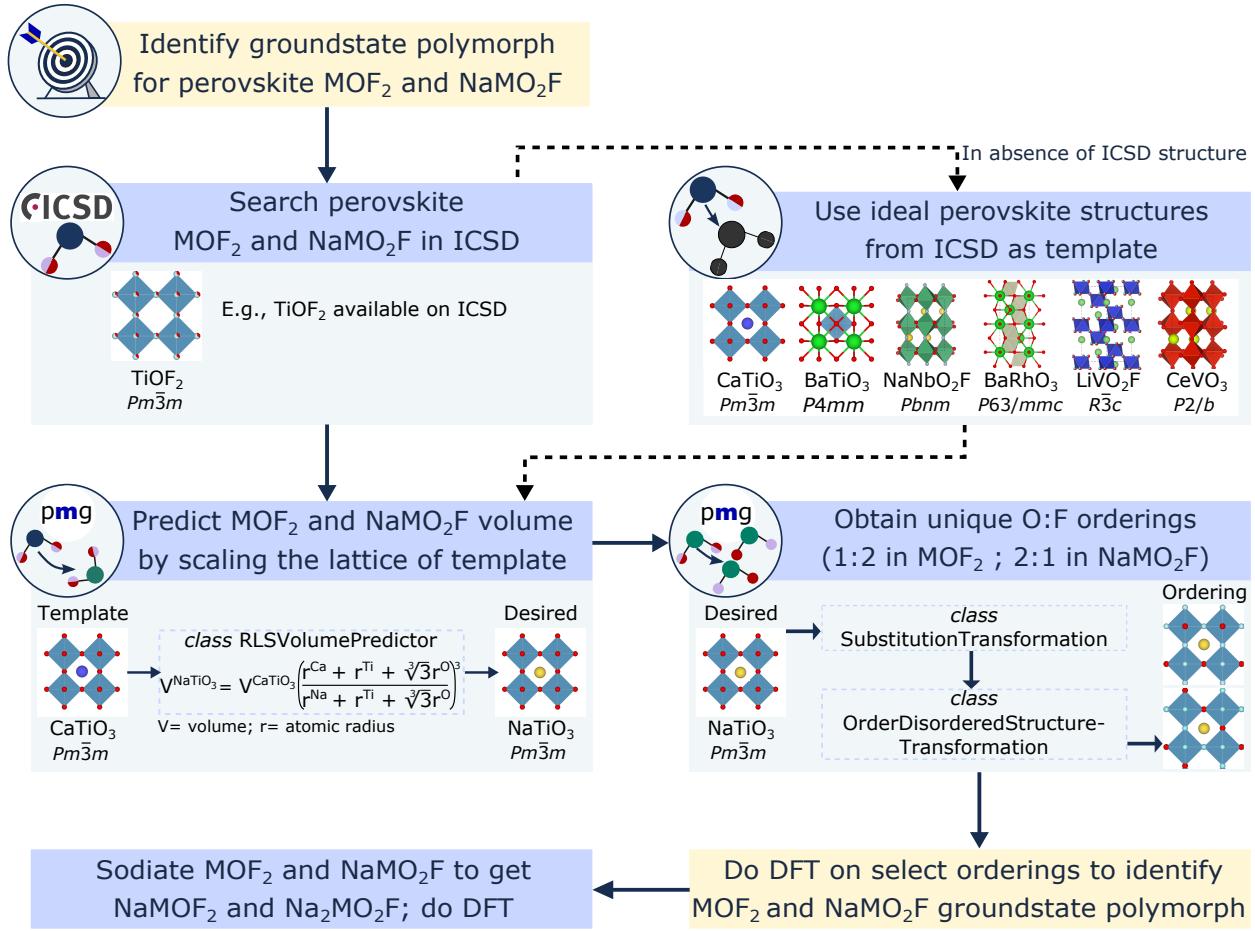
Figure 1: Workflow to obtain ground state polymorph for desodiated F-rich MOF_2 and O-rich $NaMO_2F$ perovskites, where M = Ti, V, Cr, Mn, Fe, Co, or Ni. Notations 'pmg' and 'ICSD' refer to the pymatgen package and the inorganic crystal structure database.
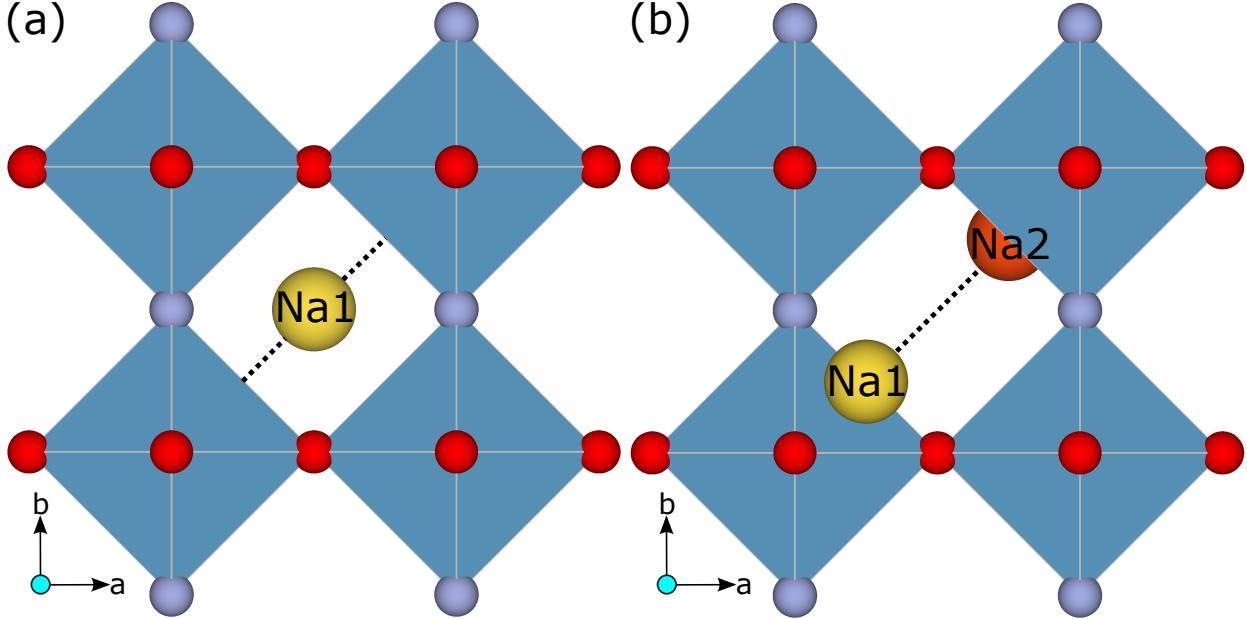
Figure 2: (a) NaTiO$_2$F with the initial Na atom (denoted by Na1) at the centre of the cube (i.e., fractional coordinates of (0.5, 0.5, 0.5)). (b) Displacement of the Na1 atom to (0.25, 0.25, 0.25) and subsequent occupation of the second Na atom (denoted by Na2) at (0.75, 0.75, 0.75). Blue polyhedra in both panels denote TiO$_4$F$_2$ octahedra. O and F are represented by red and purple spheres, respectively. Body diagonals within the cubic structures are indicated by the dotted black lines.

out of which we chose the 16 lowest electrostatic energy configurations for each space group (for both MOF$_2$ and NaMOF$_2$).

Once the ground state polymorph of each desodiated NaMO$_2$F and MOF$_2$ composition was determined, we added Na to the DFT-relaxed charged ground state structures to obtain the corresponding discharged (or sodiated) configurations, i.e., Na$_2$MO$_2$F and NaMOF$_2$. For NaMOF$_2$, we initialised the Na ions on the sites occupied by the A-cation in the corresponding template perovskite structure. Given that the NaMOF$_2$ perovskite only has one distinct Na (or A cation) site, we created a second Na site by displacing the existing Na ion to minimize electrostatic repulsion between the two Na ions, as displayed in **Figure 2**. For example, in the case of $Pm\overline{3}m$ NaTiO$_2$F, we displaced the existing Na from the centre of the cube (i.e., fractional coordinates of (0.5, 0.5, 0.5)) along the body diagonal to a new site of coordinates (0.25, 0.25, 0.25). Subsequently, we initialised the second Na atom at the coordinates of (0.75, 0.75, 0.75), to minimize electrostatic repulsions between the two Na. The introduction of additional Na sites in other perovskite structures is described in the supporting information (SI), along with a schematic in **Figure S1**.

2.2 Computational details

We used the Vienna ab initio simulation package (VASP [42,43]) for all spin-polarized DFT calculations. We utilised the projector augmented-wave (PAW [44,45]) potentials similar to our previous work, [46–48] with the list of PAW potentials used in this work compiled in **Table S1**. To account for the electronic exchange and correlation, we employed the Hubbard U corrected [49,50] strongly constrained and appropriately normed (i.e., SCAN+U) [46,47,51] functional. We utilised U values that were obtained for TMOs in our work [46,47], since they gave the best agreement between calculated and experimental average voltages in Li-based TMOFs

5

(see **Table S2**). We expanded the one-electron wavefunctions using a plane wave basis set, with a 520 eV kinetic energy cutoff, and used a Gaussian smearing of width 0.05 eV to integrate the Fermi surface. We sampled the irreducible Brillouin zone with a Γ-centered Monkhorst-pack [52] k-mesh with a density of at least 32 k-points per Å^{-1} (i.e., a minimum sampling of 32 subdivisions along each reciprocal lattice vector). For the total energies and atomic forces, we set the convergence criterion to be 0.01 meV and $|0.03|$ eV/Å^{-1}, respectively. To reduce computational complexity, we initialised all $3d$ TMs in their corresponding high-spin ferromagnetic configurations. For all structures, we relaxed the cell volume, cell shape, and ionic positions without preserving any symmetry. Where possible, we have followed a colour-blind friendly colour scheme in our plots. [53]

2.3   Ab initio thermodynamics

For evaluating the thermodynamic stability of the TMOFs considered, we constructed the 0 K convex hull of the corresponding quaternary (i.e., Na-TM-O-F) chemical spaces using the pymatgen package. Specifically, we collected experimentally-reported structures of individual elements (Na, TM, O, and F), binaries (Na-O, Na-F, TM-O, and TM-F), ternaries (Na-O-F, TM-O-F, Na-TM-O, Na-TM-F), and quaternaries (Na-TM-O-F) from the ICSD, and subsequently calculated their total energies using DFT. Note that we only considered ICSD structures that were fully ordered, i.e., each lattice site in a structure exhibits an integer occupation of a given species. Also, for individual elements, Na-O and Na-F binaries, and Na-O-F ternaries we used only the SCAN functional for treating the electronic exchange and correlation, while for the other structures we used the SCAN+U functional. Since we have utilised only DFT-calculated total energies to construct the 0 K convex hull, our phase diagrams do not include the $p-V$ contributions.

Importantly, any stable entity on the 0 K convex hull will have a energy above convex hull (E^{hull}) as 0 meV/atom, while any metastable/unstable entity will have $\text{E}^{hull}>0$. [54] Given that compounds that are metastable at 0 K can be stabilised under different experimental conditions, we used a synthesizeability threshold of $\text{E}^{hull}\leq100$ meV/atom. [55] This implies that compounds with a $\text{E}^{hull}\leq100$ meV/atom may be synthesizeable under higher temperatures/pressures, and can be considered metastable, while compounds with $\text{E}^{hull}>100$ meV/atom are unlikely to be synthesizeable and can be considered to be unstable. All calculated phase diagrams (except for the Na-Ti-O-F quaternary) are compiled in **Figure S3**, while the list of stable/unstable compounds are compiled in **Table S4**.

The average voltage for Na (de)intercalation in TMOFs is evaluated using DFT-based total energies from the well-known Nernst equation. [56] Considering a Na (de)intercalation reaction of the form, $\text{Na}_x\text{TMOF} + \Delta x\text{Na} \leftrightarrow \text{Na}_{x+\Delta x}\text{TMOF}$, we can approximate the Gibbs energy change (ΔG) associated with the (de)intercalation process using **Equation 1**, which neglects entropic and $p-V$ contributions. Note that the E terms in **Equation 1** are DFT-calculated, with Na_xTMOF and $\text{Na}_{x+\Delta x}\text{TMOF}$ described with SCAN+U and metallic Na described with SCAN in its body-centered-cubic ground state. F is Faraday's constant.

$$\langle V \rangle = \frac{\Delta G}{\Delta x \ F} \approx -\frac{E(\text{Na}_{x+\Delta x}\text{TMOF}) - [E(\text{Na}_x\text{TMOF}) + \Delta x \ E(\text{Na})]}{\Delta x \ F} \tag{1}$$

2.4   Kinetics

To estimate the ionic mobility of Na$^+$ in select TMOF frameworks, we utilized DFT-based nudged elastic band (NEB [57,58]) calculations to estimate the migration barrier (E_m) associated with Na$^+$ motion. For all structures, we considered a vacancy-mediated Na$^+$ migration along the A-site 'tunnel' of the perovskite

6

framework, and calculated E_m either at the charged or the discharged sodium concentration limits. Upon introducing a Na-vacancy and fully relaxing the endpoint configurations, we interpolated five images across the endpoints to initialise the minimum energy path (MEP).

Spring forces of 5 eV/Å were introduced between the images, and we considered the NEB calculation converged when the total energy of each image and the perpendicular component of the force between each image dropped below 0.01 meV and $|0.05|$ eV/Å, respectively. For all NEB calculations, we used supercells with lattice parameters ≥ 8 Å to avoid spurious interactions of the migrating Na with its periodic images. We used the Perdew-Burke-Ernzerhof (PBE [59]) parameterization of the generalized gradient approximation (GGA) to describe the exchange-correlation in our NEB calculations instead of SCAN, since GGA provides accurate qualitative trends at lower computational cost and with fewer convergence difficulties. [60] All computed MEPs are compiled in **Figure S4**.

3 Results

3.1 Ground state polymorphs and average voltages

The ground state polymorph for each desodiated F-rich MOF_2 and O-rich $NaMO_2F$ are represented by the black arrows in panels a and b of **Figure 3**. The percentage normalised differences in energies of the other polymorphs considered, relative to the ground state, are plotted as bars in **Figure 3**. Specifically, we have plotted the percentage differences, calculated as $\frac{E(\text{polymorph})-E(\text{groundstate})}{E(\text{highest}-\text{energy}-\text{polymorph})-E(\text{groundstate})} \times 100$, where each concentric ring on the radars represent percentage steps of 20%. Thus, the ground state and the highest energy polymorph represent 0% and 100%, respectively, on the radars of **Figure 3** for each composition. Notably, the ground state polymorphs of the MOF_2 compositions include $Pbnm$ (for Ti, V, Fe), $R\bar{3}c$ (Cr, Mn, Ni), and $P2/b$ (Co), while for the $NaMO_2F$ compositions are $P2/b$ (Ti, V, Mn, Fe, Co), $Pbnm$ (Cr), and $R\bar{3}c$ (Ni). We have compiled the percentage normalised relative energies for all perovskite polymorphs considered in **Table S3** and provided schematics of the desodiated ground states and their corresponding sodiated structures in **Figure S2**.

Figure 4 depicts the calculated average voltages for Na (de)intercalation, versus Na/Na^+, into the ground state polymorphs of F-rich MOF_2 (orange bars) and O-rich $NaMO_2F$ (blue bars). The extent of Na (de)intercalation considered in both F-rich and O-rich perovkistes are one Na per f.u., corresponding to $MOF_2 \leftrightarrow NaMOF_2$ and $NaMO_2F \leftrightarrow Na_2MO_2F$, respectively. Expectedly, we find the F-rich perovskites to exhibit consistently higher average voltages than the corresponding O-rich perovskites, which can be attributed to the greater inductive effect of F^- compared to O^{2-}. [20] Indeed, fluorine's inductive effect causes an increase in average voltage of ≥ 2 V for all TM (except Mn at a 1.98 V increase), with the increase in Ni being the highest at 3.08 V.

In both the F-rich and O-rich perovskites, there is a monotonic increase in voltages along the $3d$ series, with the values increasing from 2.21 V (in Ti) to 4.78 V (Ni) in F-rich, and -0.13 V (Ti) to 2.68 V (Co) in O-rich. The monotonic trends in voltages can be largely attributed to the corresponding trends in standard reduction potentials of the TMs. [61] The dip in voltage from Co to Ni in O-rich perovskites can be primarily attributed to cooperative Jahn-Teller distortion in the Ni-perovskite, which results in a larger deviations in lattice parameters (see compiled b/a and c/a ratios in Mn- and Ni-perovskites in **Table S5**). Interestingly, the average intercalation voltage in the O-rich Ti-perovskite exhibits a negative value (-0.13 V), indicating non-spontaneity of Na-intercalation in this system. This is because the intercalated Na_2TiO_2F is
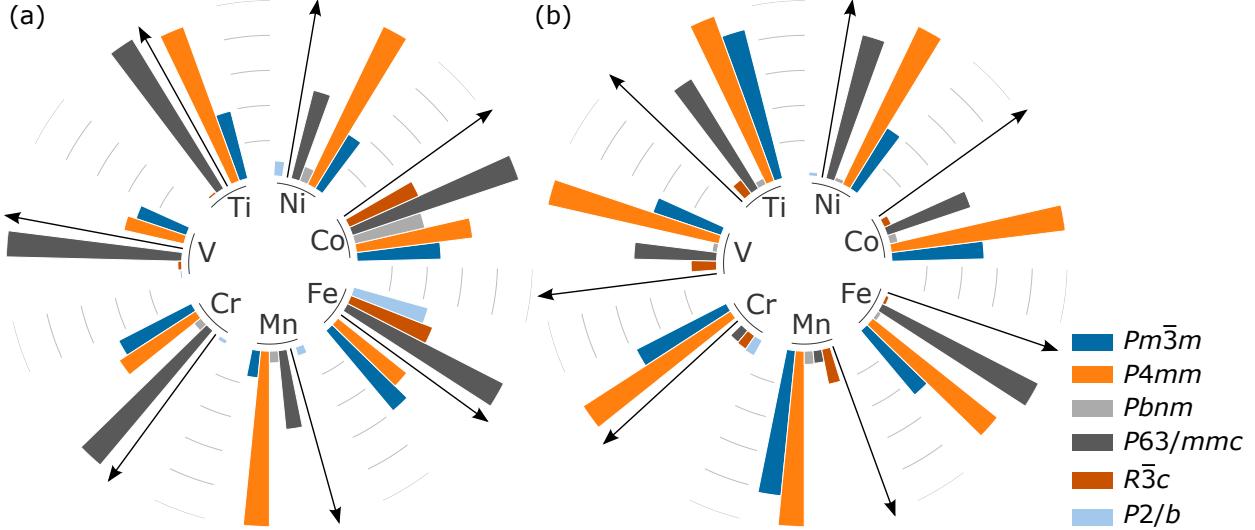
Figure 3: Percentage normalised relative energies of all polymorphs considered with respect to the corresponding ground states for (a) F-rich MOF_2 and (b) O-rich $NaMO_2F$. All ground state polymorphs are indicated by black arrows. Each concentric ring on the radars represent a percentage step of 20%.

thermodynamically unstable, with Na-metal being one of the decomposition products (see **Figure 5**).

Given the electrolyte stability windows of liquid electrolytes in NIBs typically span up to 4.8 V vs. Na/Na^+, [62,63] we find all perovskites considered in this work to be suitable as NIB electrodes. The low average voltages of several O-rich perovskites, including V, Cr, Mn, and Fe (<2.5 V), and $TiOF_2$, make these systems more suitable as negative electrodes (anodes) than cathodes in a NIB. Thus, based on the voltage data alone, we find the Mn-, Fe-, Co-, and Ni-based F-rich perovskites to be the most promising as NIB cathodes. However, practical deployment of candidate electrode materials in NIBs will be highly dependent on their synthesizability (i.e., thermodynamic stability) and their rate performance (i.e., Na-ion mobility).

3.2   Thermodynamic stability

Upon construction of the quaternary 0 K Na-TM-O-F convex hulls, we plotted pseudo-ternary slices (or projections) of the quaternary phase diagram for each TM for ease of visualization. For instance, ternary projections of the Na-Ti-O-F system is displayed in **Figure 5**, while the ternary projections for the remaining TM systems are compiled in **Figure S3**. The background colors in all panels (shades of green) of **Figure 5** indicate the energy of formation ($E^{formation}$), calculated with respect to the terminating compositions of the ternary projections. Stable compounds within the ternary projections are indicated by black circles. Metastable/unstable compounds are indicated by red diamonds. For each metastable/unstable compound among the TMOFs considered, the set of decomposition products (i.e., stable compounds that a metastable/unstable compound is thermodynamically driven to decomposes into) is compiled in **Table S6**.

For visualising the $TiOF_2$ composition in the Ti-quaternary, we used a ternary projection terminated by TiO_2, TiF_3, and O_2 (see **Figure 5a**). Similarly, for visualizing the $NaTiOF_2$, we used the $NaTiF_4$-NaF-Ti_2O_3 ternary projection (**Figure 5b**). Both $NaTiO_2F$ and Na_2TiO_2F can be captured within the TiO_2-NaF-Na projection **Figure 5c**. Importantly, **Figure 5** indicates that $TiOF_2$ is thermodynamically stable (E^{hull} =0 meV/atom), $NaTiOF_2$, and $NaTiO_2F$ are metastable with E^{hull} of 46, and 53 meV/atom, respectively, which are below the 100 meV/atom threshold, and Na_2TiO_2F is unstable with E^{hull} of 187 meV/atom.
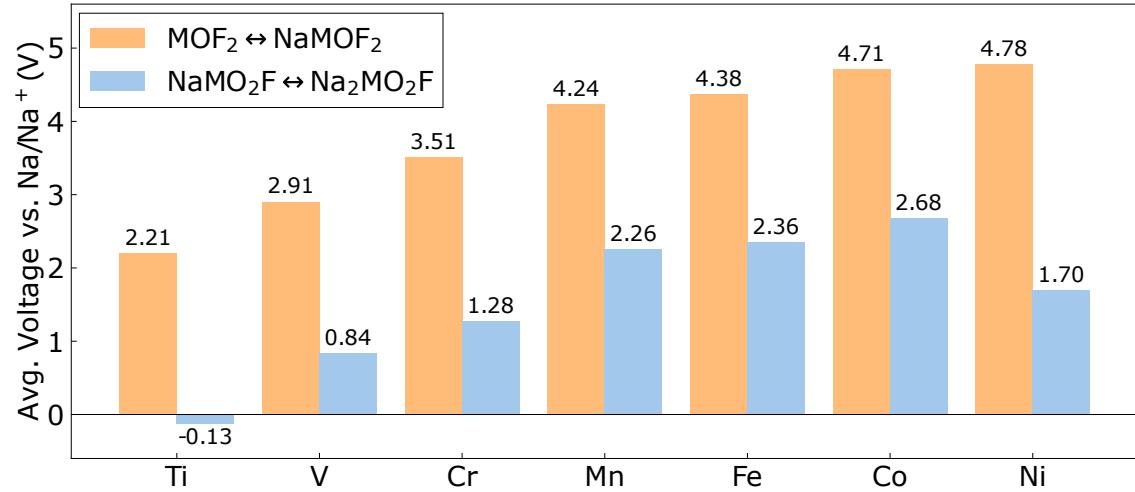
Figure 4: Calculated average Na (de)intercalation voltages (in V), versus Na/Na$^+$, in F-rich (orange bars) and O-rich (blue bars) TMOFs considered.
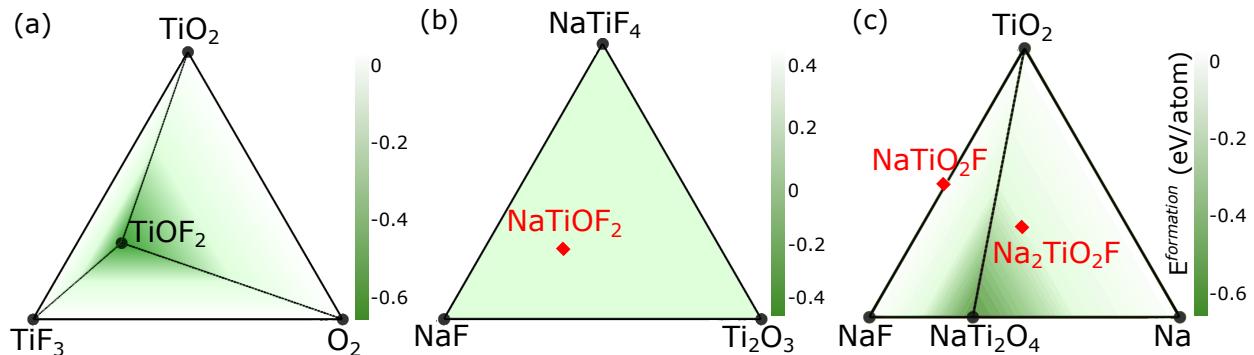

Figure 5: Ternary projections of Na-Ti-O-F phase diagram to visualise (a) TiOF$_2$, (b) NaTiOF$_2$, and (c) NaTiO$_2$F and Na$_2$TiO$_2$F. In each panel, the green-to-white background represents E^{formation}, while the red diamonds indicate meta/instability (E^{hull} >0). Black circles indicate stable compositions and black lines are tie-lines.
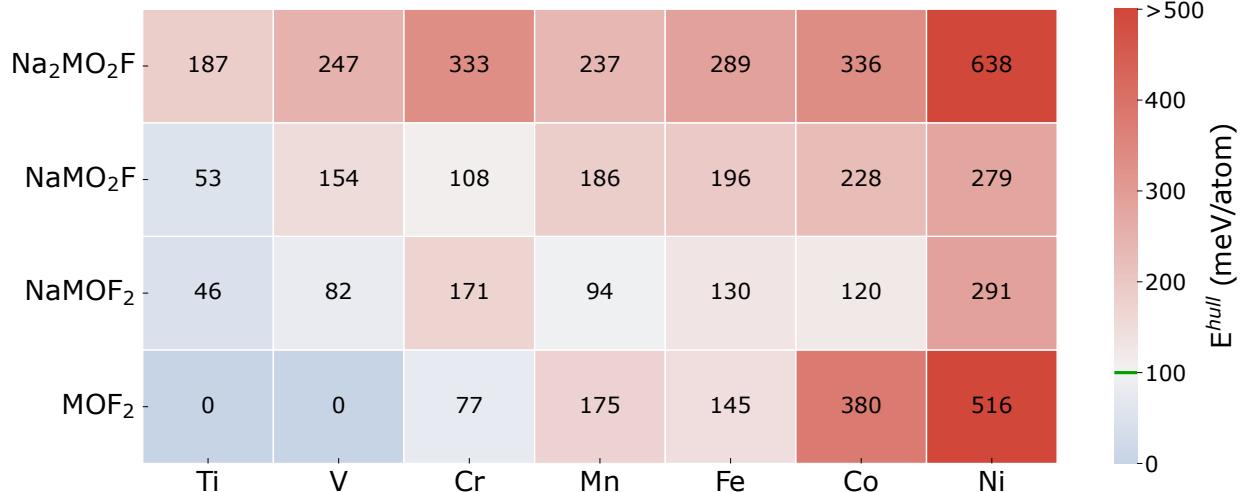
Figure 6: Calculated E^{hull}) for charged and discharged F-rich TMOFs (bottom two rows) and O-rich TMOFs (top two rows). Each column represents a $3d$ TM, while the E^{hull} for each compound is indicated using text annotations within each square. The green line on the legend bar indicates the 100 meV/atom synthesizability threshold considered in this work.

Notably, Na-metal is one of the decomposition products for the unstable Na_2TiO_2F (**Figure 5c**), which explains the calculated negative intercalation voltage for the $NaTiO_2F \leftrightarrow Na_2TiO_2F$ reaction (**Figure 4**).

The heatmap depicted of **Figure 6** compiles the E^{hull} data of all charged and discharged O-rich and F-rich perovskites considered. Blue squares indicate stable/metastable compounds, while red squares indicate unstable compounds. The text annotations within each square represents the E^{hull} in meV/atom for the corresponding compound. Significantly, we find only $TiOF_2$ and VOF_2 to be thermodynamically stable (i.e., E_{hull} =0 meV/atom) among all the TMOFs considered. This is in agreement with experimental reports that have synthesized $TiOF_2$ [27] and VOF_2. [64] All charged and discharged compositions of Fe-, Co-, and Ni-based TMOFs are unstable, with E^{hull} greater than the synthesizability threshold of 100 meV/atom, citing the high unsuitability of such compositions as NIB electrodes. Moreover, all O-rich perovskites, except $NaTiO_2F$, exhibit E^{hull} >100 meV/atom, highlighting their high instabilities.

While it is good for an electrode to have thermodynamically stable charged and discharged states to avoid any irreversible decomposition or conversion reactions during an electrochemical cycle, topotactic (de)intercalation is often possible with metastable charged and discharged states as well. [65–68] Thus, compositions that lie within the E^{hull} threshold of 100 meV/atom can be considered as possible electrodes. Thus, possible structures that can be considered as NIB electrodes, given thermodynamic stability constraints, include $TiOF_2$-$NaTiOF_2$, VOF_2-$NaVOF_2$, $CrOF_2$, and $NaMnOF_2$, and the ease of Na-ion mobility within these frameworks will further determine their suitability. Note that the high instabilities of $NaCrOF_2$ and $MnOF_2$ may limit the Na insertion/extraction capacity in these electrodes, compared to $TiOF_2$-$NaTiOF_2$, and VOF_2-$NaVOF_2$. Although we find $NaTiO_2F$ to be metastable, we did not calculate Na E_m within this structure given the negative average intercalation voltage associated with Na_2TiO_2F formation.

3.3 Ionic mobility

For the candidate compositions identified via our voltage and stability calculations, we estimated the Na E_m via the vacancy-mediated mechanism, and compiled the values in **Figure 7**. Barriers calculated
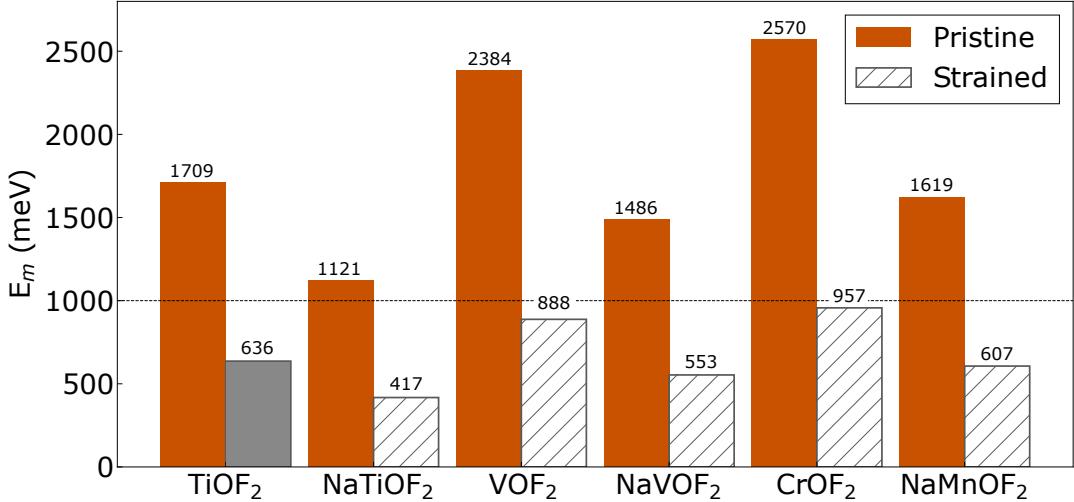
Figure 7: GGA-calculated E_m of pristine (solid orange bars) and strained (solid grey or hashed bars) candidate compositions. The horizontal dotted line indicates the threshold E_m of 1000 meV.

in regular TMOF compositions are represented by solid orange bars in **Figure 7**, while barriers calculated in strained compositions (*vide infra*) are indicated by solid grey or hatched bars. We used a threshold value of 1000 meV for the E_m, indicated by the dotted black line in **Figure 7**, to represent an electrode material that can be used in reasonable electrochemical conditions, similar to our previous works. [67, 69] Thus, electrodes that exhibit $E_m \leq 1000$ meV are considered candidates for further experimental exploration. Notably, all shortlisted TMOF compositions exhibit barriers that are above the 1000 meV threshold in their pristine state. Only $NaTiOF_2$, with a barrier of 1121 meV, is close to the 1000 meV threshold, with other compositions exhibiting significantly higher E_m, including $NaVOF_2$ (1486 meV), $NaMnOF_2$ (1619 meV), $TiOF_2$ (1709 meV), VOF_2 (2384 meV), and $CrOF_2$ (2570 meV).

Introducing strain in an electrode can often lead to lowering of E_m and consequent increasing in ionic mobility. [70–72] Thus, to examine whether the identified TMOFs can reasonably function as NIB electrodes under strain, we introduced a homogeneous tensile strain of 5% across all lattice parameters of $TiOF_2$ and evaluated the Na-E_m using GGA-based NEB. To ensure that the tensile strain is maintained during structural relaxation, we restricted the relaxation of the end points to only include changes in ionic positions. Importantly, the strain introduction significantly reduced the E_m to 636 meV (i.e., by 62.8%) compared to the pristine-$TiOF_2$, as shown by the solid gray bar in **Figure 7**.

Assuming similar reductions in calculated E_m with strain addition in other TMOFs (i.e., by 62.8% compared to the pristine-case), we estimate the barriers in strained $NaTiOF_2$, VOF_2, $NaVOF_2$, $CrOF_2$, and $NaMnOF_2$ to be 417 meV, 888 meV, 553 meV, 957 meV, and 607 meV, respectively (see hashed bars in **Figure 7**). Thus, all TMOFs identified using our voltage and stability criteria may exhibit reasonable Na-ionic mobility, provided a homogeneous strain is introduced within the materials. In practice, lattice expansion can be achieved through doping, [73,74] heat/mechanical treatment, [75,76] and/or epitaxially, such as in the case of thin film electrodes. [71,77] Note that introducing strain and maintaining it during electrochemical cycling may come at the cost of energy density of the eventual battery. Thus, we expect $TiOF_2$-$NaTiOF_2$, VOF_2-$NaVOF_2$, $CrOF_2$, and $NaMnOF_2$ to be NIB electrodes worth exploring experimentally, especially for strained electrode configurations and thin film batteries.

4   Discussion

In this work, we performed first principles calculations to explore the scope of $3d$ TM-based F- and O-rich perovskite oxyfluorides (Na_xMOF_2 and $Na_{1+x}MO_2F$, $x=$ 0-1) as NIB electrodes. Using a structural template based workflow, we identified the ground state polymorphs of the charged MOF_2 and $NaMO_2F$ compositions (M = Ti, V, Cr, Mn, Fe, Co, or Ni) among six possible space groups commonly adopted by perovskites. Subsequently, we introduced Na to create corresponding discharged perovskite compositions, namely $NaMOF_2$ and Na_2MO_2F, and evaluted the average Na (de)intercalation voltages, 0 K thermodynamic stabilities in all perovskites, and Na-ion mobility in a select set of candidate perovskites. Based on our voltage, stability, and mobility calculations, we identify six perovskite compositions, namely $TiOF_2$-$NaTiOF_2$, VOF_2-$NaVOF_2$, $CrOF_2$, and $NaMnOF_2$ to hold some promise as NIB electrodes, if used in strained configurations and/or in thin film batteries.

During the process of enumerating possible structures for the charged perovskites, we only considered a maximum of 16 lowest electrostatic energy configurations within each space group, and identified the ground state configuration among these structures as the one with the lowest DFT total energy (per f.u.). Note that the choice of the 16 lowest electrostatic energy structures (per space group) is an approximation and there is always a non-zero chance of encountering the 'true' ground state beyond this choice. Using our criteria of a maximum of 16 structures per space group contributes to a total of 72 structures per perovskite composition (i.e., $16 \times 4 + 5 + 3$), which in turn adds up to 1008 structures over all TMs considered and over both O-rich and F-rich compositions, which by itself represents a significant computational expense. Nevertheless, even if the 'true' ground state is beyond the set of configurations we have considered here, we expect it to exhibit a lower energy, of the order of $\sim$10 meV/f.u., compared to the ground state that we have identified, which will only cause a marginal change to the voltage ($\sim$10 mV) and stability ($E^{hull} \pm 10$ meV/f.u.) predictions.

Another approximation in our structure generation workflow is the identification of ground state configurations at the charged perovskite compositions followed by addition of Na to the lowest-energy charged structure to obtain the discharged structure. We could have followed a similar procedure of ground state identification using the discharged composition instead of the charged composition. Our choice of the charged perovskite composition for ground state identification was motivated largely by experimental reports on TMOFs in LIBs, wherein, Li was typically inserted into charged TMOF compositions. [27, 28] Thus, the TMOF composition was synthesized first followed by Li discharge to obtain the discharged state. Considering the ground state configuration at the discharged state may lead to qualitatively different results, in terms of average voltages, 0 K stability, and Na-ionic mobility. But considering a workflow along the discharged compositions represents a significant computational effort, which we plan to take up as future work.

For all SCAN+U calculations, we used the U value derived from TM oxides since the oxide-based U better reproduced the experimentally determined voltages for Li-intercalation in TMOFs, such as $VO_2F \leftrightarrow LiVO_2F$ and $TiOF_2 \leftrightarrow Li_{0.5}TiOF_2$. [27,28] Hence, we did not tailor our U values specifically for oxyfluorides. More experimental data will be needed to verify if such tailored U values will yield more accurate predictions. Additionally, we initialised all our TMs in their corresponding ferromagnetic high-spin configurations, and did not consider possible magnetic/spin orderings due to their computational complexity, which may have marginally affected the set of ground states that we obtained. Also, SCAN+U is known to overestimate intercalation voltages and meta/instability of compounds, [78] which is also a reason for us to consider a fairly large threshold ($E^{hull} \leq 100$ meV/atom) for synthesizability.

We used a reasonably high threshold for ionic mobility ($E_m \leq 1000$ meV [67]) to identify candidates partly due to the limited literature on Na-ion mobility within crystalline ordered oxyfluorides. Moreover, addition

of F^- to oxides can result in a reduction of Na^+ mobility due to more ionic Na-F bonds than Na-O, similar to observations of reduction in Li-mobility in F-doped oxide-based disordered rocksalts. [79,80] Importantly, our calculations indicated that only $NaTiOF_2$ (E_m =1121 meV) came close to the threshold used, with all other oxyfluorides considered exhibiting significantly high E_m Na-motion. However, introducing a homogenous strain ($\sim$5%) within the lattice can significantly reduce the E_m (by $\sim$60%), as demonstrated for the case of $TiOF_2$. Thus, TMOFs can exhibit reasonable rate performance under lattice strain. However, the need to maintain the strained structure may limit the applicability of TMOFs to low power and/or thin film batteries that are typically used in internet-of-things applications and wearable electronics.

Considering the oxyfluoride compositions of Na_xMOF_2 and $Na_{1+x}MO_2F$ was primarily motivated by the availability of the $M^{4+/3+}$ redox couple, which is exhibited by several $3d$ TMs, quite reversibly. Our work can be extended to other fluorine-added compositions, such as F-substituted oxides, phosphates, sulphates, and pyrophosphates. Indeed, high voltages and capacities with Na (de)intercalation have already been reported in fluorophosphates. [81–83] Therefore, we are hopeful that our research lays the foundation for exploring other promising compositions for NIB electrodes within and beyond the chemical space of oxyfluorides.

5   Conclusion

NIBs, which represent an alternative technological pathway to the state-of-the-art LIBs in energy storage technology, require novel materials to improve the energy and power densities so that NIBs compete better with LIBs. Here, we explored the chemical space of perovskite-based TMOFs, considering both O-rich and F-rich compositions, as possible Na-ion intercalation hosts. Specifically, we performed DFT-based calculations on Na_xMOF_2 and $Na_{1+x}MO_2F$ (x = 0-1), where M = Ti, V, Cr, Mn, Fe, Co, or Ni, evaluating the ground state polymorphs, average Na (de)intercalation voltages, 0 K stabilities, and Na^+ mobilities. We found that F-rich perovskites exhibit higher voltages than O-rich compositions, due to the stronger inductive effect of F^-. In terms of stability, only $TiOF_2$ and VOF_2 were stable while other compositions, including $NaTiOF_2$, $NaVOF_2$, $CrOF_2$ and $NaMnOF_2$ were metastable ($E^{hull} \leq 100$ meV/atom). However, all stable and metastable TMOFs exhibited high E_m ($\geq$1000 meV) for Na^+ motion in their pristine states. Nevertheless, introducing a 5% homogenous tensile strain causes the E_m to drop by $\sim$60% compared to the pristine state, suggesting that the TMOFs may have applications in thin film batteries and in strained electrode configurations. Our study represents a systematic computational exploration of the oxyfluoride chemical space, which we hope will reinvigorate research in these chemistries for NIBs and beyond.

Conflicts of Interest

There are no conflicts to declare.

Supplementary Materials

Electronic Supporting Information is available online at , Details of PAW potentials used, description of site determination for introducing additional Na in perovskites, compilation of 0 K phase diagrams and associated stability data, all calculated MEPs.

6 Data and code availability

The data that support the findings of this study are openly available at our GitHub repository.

References

[1] Kudakwashe Chayambuka, Grietus Mulder, Dmitri L Danilov, and Peter HL Notten. From li-ion batteries toward na-ion chemistries: challenges and opportunities. *Advanced energy materials*, 10(38):2001310, 2020.

[2] Christoph Vaalma, Daniel Buchholz, Marcel Weil, and Stefano Passerini. A cost and resource analysis of sodium-ion batteries. *Nature reviews materials*, 3(4):1–11, 2018.

[3] Jiaolong Zhang, Wenhui Wang, Wei Wang, Shuwei Wang, and Baohua Li. Comprehensive review of p2-type $na_{2/3}ni_{1/3}mn_{2/3}o_2$, a potential cathode for practical application of na-ion batteries. *ACS applied materials & interfaces*, 11(25):22051–22066, 2019.

[4] Jun Xiao, Xiao Li, Kaikai Tang, Dandan Wang, Mengqi Long, Hong Gao, Weihua Chen, Chuntai Liu, Hao Liu, and Guoxiu Wang. Recent progress of emerging cathode materials for sodium ion batteries. *Materials Chemistry Frontiers*, 5(10):3735–3764, 2021.

[5] Sung-Wook Kim, Dong-Hwa Seo, Xiaohua Ma, Gerbrand Ceder, and Kisuk Kang. Electrode materials for rechargeable sodium-ion batteries: potential alternatives to current lithium-ion batteries. *Advanced Energy Materials*, 2(7):710–721, 2012.

[6] Ashish Rudola, Ruth Sayers, Christopher J Wright, and Jerry Barker. Opportunities for moderate-range electric vehicles using sustainable sodium-ion batteries. *Nature Energy*, 8(3):215–218, 2023.

[7] J Barker and CJ Wright. Storage and/or transportation of sodium-ion cells. *US*, 237270:A1, 2017.

[8] Xiaolong Li, XinXin Zhang, Wenguang Lin, Xiaoxia Chen, Ben Liu, Shikang Yao, and Jiadian Lan. Secondary battery, battery module, battery pack, and electric apparatus, February 8 2024. US Patent App. 18/489,849.

[9] Hayley S Hirsh, Yixuan Li, Darren HS Tan, Minghao Zhang, Enyue Zhao, and Y Shirley Meng. Sodium-ion batteries paving the way for grid energy storage. *Advanced Energy Materials*, 10(32):2001274, 2020.

[10] Fanglin Wei, Qiaoping Zhang, Peng Zhang, Wenqian Tian, Kehua Dai, Liang Zhang, Jing Mao, and Guosheng Shao. Research progress on layered transition metal oxide cathode materials for sodium ion batteries. *Journal of The Electrochemical Society*, 168(5):050524, 2021.

[11] Jae Chul Kim, Deok-Hwang Kwon, Julia H Yang, Hyunchul Kim, Shou-Hang Bo, Lijun Wu, Haegyeom Kim, Dong-Hwa Seo, Tan Shi, Jingyang Wang, et al. Direct observation of alternating octahedral and prismatic sodium layers in o3-type transition metal oxides. *Advanced Energy Materials*, 10(31):2001151, 2020.

[12] Debolina Deb and Gopalakrishnan Sai Gautam. Critical overview of polyanionic frameworks as positive electrodes for na-ion batteries. *Journal of Materials Research*, 37(19):3169–3196, 2022.

[13] Sathiya Mariyappan, Qing Wang, and Jean Marie Tarascon. Will sodium layered oxides ever be competitive for sodium ion battery applications? *Journal of The Electrochemical Society*, 165(16):A3714, 2018.

[14] Mingyue Tian, Lan Xu, and Ya Yang. Perovskite oxide ferroelectric thin films. *Advanced Electronic Materials*, 8(7):2101409, 2022.

[15] Songbo Ye, Jinpeng Zhu, Saisai Zhu, Yang Zhao, Mingliang Li, Zhihao Huang, Hailong Wang, and Jilin He. Design strategies for perovskite-type high-entropy oxides with applications in optics. *ACS applied materials & interfaces*, 15(40):47475–47486, 2023.

[16] Eman Abdul Rahman Assirey. Perovskite synthesis, properties and their related biochemical and industrial application. *Saudi Pharmaceutical Journal*, 27(6):817–829, 2019.

[17] Azhar Fakharuddin, Mahesh K Gangishetty, Mojtaba Abdi-Jalebi, Sang-Hyun Chin, Abd Rashid bin Mohd Yusoff, Daniel N Congreve, Wolfgang Tress, Felix Deschler, Maria Vasilopoulou, and Henk J Bolink. Perovskite light-emitting diodes. *Nature Electronics*, 5(4):203–216, 2022.

[18] Gopalakrishnan Sai Gautam, Ellen B Stechel, and Emily A Carter. Exploring ca–ce–m–o (m= 3d transition metal) oxide perovskites for solar thermochemical applications. *Chemistry of Materials*, 32(23):9964–9982, 2020.

[19] Hayden A Evans, Yue Wu, Ram Seshadri, and Anthony K Cheetham. Perovskite-related reo$_3$-type structures. *Nature Reviews Materials*, 5(3):196–213, 2020.

[20] Yiqing Wang, Zhenzhen Wu, Faezeh Makhlooghi Azad, Yutong Zhu, Lianzhou Wang, Craig J Hawker, Andrew K Whittaker, Maria Forsyth, and Cheng Zhang. Fluorination in advanced battery design. *Nature Reviews Materials*, 9(2):119–133, 2024.

[21] A Manthiram and JB Goodenough. Lithium insertion into $fe_2(so_4)_3$ frameworks. *Journal of Power Sources*, 26(3-4):403–408, 1989.

[22] Akshaya K Padhi, Kirakodu S Nanjundaswamy, and John B Goodenough. Phospho-olivines as positive-electrode materials for rechargeable lithium batteries. *Journal of the electrochemical society*, 144(4):1188, 1997.

[23] Guochun Yan, Sathiya Mariyappan, Gwenaelle Rousse, Quentin Jacquet, Michael Deschamps, Renald David, Boris Mirvaux, John William Freeland, and Jean-Marie Tarascon. Higher energy and safer sodium ion batteries via an electrochemically made disordered $na_3v_2(po_4)_2f_3$ material. *Nature communications*, 10(1):585, 2019.

[24] Long HB Nguyen, Antonella Iadecola, Stéphanie Belin, Jacob Olchowka, Christian Masquelier, Dany Carlier, and Laurence Croguennec. A combined operando synchrotron x-ray absorption spectroscopy and first-principles density functional theory study to unravel the vanadium redox paradox in the $na_3v_2(po_4)_2f_3$–$na_3v_2(po_4)_2fo_2$ compositions. *The Journal of Physical Chemistry C*, 124(43):23511–23522, 2020.

[25] Mainul Akhtar, Hafssa Arraghraghi, Sylvia Kunz, Qingsong Wang, and Matteo Bianchini. A novel solid-state synthesis route for high voltage $na_3v_2(po\ 4)_2f_{3-2y}o_{2y}$ cathode materials for na-ion batteries. *Journal of Materials Chemistry A*, 11(46):25650–25661, 2023.

[26] Da Deng. Transition metal oxyfluorides for next-generation rechargeable batteries. *ChemNanoMat*, 3(3):146–159, 2017.

[27] MV Reddy, S Madhavi, GV Subba Rao, and BVR Chowdari. Metal oxyfluorides $tiof_2$ and nbo_2f as anodes for li-ion batteries. *Journal of power sources*, 162(2):1312–1321, 2006.

[28] Alois Kuhn, Michael R Plews, Juan Carlos Pérez-Flores, François Fauth, Markus Hoelzel, Jordi Cabana, and Flaviano García-Alvarado. Redox chemistry and reversible structural changes in rhombohedral vo_2f cathode during li intercalation. *Inorganic chemistry*, 59(14):10048–10058, 2020.

[29] Xiaoya Wang, Yuh-Chieh Lin, Hui Zhou, Fredrick Omenya, Iek-Heng Chu, Khim Karki, Shawn Sallis, Jatinkumar Rana, Louis FJ Piper, Natasha A Chernova, et al. Structural changes in a high-energy density vo_2f cathode upon heating and li cycling. *ACS Applied Energy Materials*, 1(9):4514–4521, 2018.

[30] Xiaoyu Xu, Liquan Pi, John-Joseph Marie, Gregory J Rees, Chen Gong, Shengda Pu, Robert A House, Alexander W Robertson, and Peter G Bruce. Li_2nio_2f a new oxyfluoride disordered rocksalt cathode material. *Journal of The Electrochemical Society*, 168(8):080521, 2021.

[31] Yasaman Shirazi Moghadam, Abdel El Kharbachi, Yang Hu, Kai Wang, Stéphanie Belin, and Maximilian Fichtner. Na-rich disordered rock salt oxyfluoride cathode materials for sodium ion batteries. *ACS Materials Letters*, 5(1):125–132, 2022.

[32] Juan Carlos Pérez-Flores, Raquel Villamor, David Ávila-Brande, José M Gallardo Amores, Emilio Morán, Alois Kuhn, and Flaviano García-Alvarado. Vo_2f: a new transition metal oxyfluoride with high specific capacity for li ion batteries. *Journal of materials chemistry A*, 3(41):20508–20515, 2015.

[33] Ruiyong Chen, Emad Maawad, Michael Knapp, Shuhua Ren, Přemysl Beran, Raiker Witter, and Rolf Hempelmann. Lithiation-driven structural transition of vo$_2$f into disordered rock-salt li$_x$vo$_2$f. *Rsc Advances*, 6(69):65112–65118, 2016.

[34] Ekaterina V Astrova, Vladimir P Ulin, Alesya V Parfeneva, Galina V Li, Maria A Yagovkina, Darina A Lozhkina, Andrei A Krasilin, Maria V Tomkovich, and Aleksander M Rumyantsev. Titanium oxyfluoride as a material for negative electrodes of lithium-ion batteries. *International Journal of Molecular Sciences*, 24(5):4968, 2023.

[35] Ayuko Kitajou, Liwei Zhao, Rintaro Nagano, Atsushi Inoishi, Eiji Kobayashi, and Shigeto Okada. Electrochemical performance and thermal stability of iron oxyfluoride (feof) for sodium-ion batteries. *Batteries*, 4(4):68, 2018.

[36] RJ Clément, Z Lun, and G Ceder. Cation-disordered rocksalt transition metal oxides and oxyfluorides for high energy lithium-ion cathodes. *Energy & Environmental Science*, 13(2):345–373, 2020.

[37] Jianchao Ye, Patrick Shea, Andreas C Baumgaertel, Stanimir A Bonev, Monika M Biener, Michael Bagge-Hansen, Y Morris Wang, Juergen Biener, and Brandon C Wood. Amorphization as a pathway to fast charging kinetics in atomic layer deposition-derived titania films for lithium ion batteries. *Chemistry of Materials*, 30(24):8871–8882, 2018.

[38] Mariette Hellenbrandt. The inorganic crystal structure database (icsd)—present and future. *Crystallography Reviews*, 10(1):17–22, 2004.

[39] C Heubner, S Heiden, M Schneider, and A Michaelis. In-situ preparation and electrochemical characterization of submicron sized nafepo$_4$ cathode material for sodium-ion batteries. *Electrochimica Acta*, 233:78–84, 2017.

[40] Iek-Heng Chu, Sayan Roychowdhury, Daehui Han, Anubhav Jain, and Shyue Ping Ong. Predicting the volumes of crystals. *Computational Materials Science*, 146:184–192, 2018.

[41] Paul P Ewald. Die berechnung optischer und elektrostatischer gitterpotentiale. *Annalen der physik*, 369(3):253–287, 1921.

[42] Georg Kresse and Jürgen Furthmüller. Efficiency of ab-initio total energy calculations for metals and semiconductors using a plane-wave basis set. *Computational materials science*, 6(1):15–50, 1996.

[43] Georg Kresse and Jürgen Furthmüller. Efficient iterative schemes for ab initio total-energy calculations using a plane-wave basis set. *Physical review B*, 54(16):11169, 1996.

[44] Georg Kresse and Daniel Joubert. From ultrasoft pseudopotentials to the projector augmented-wave method. *Physical review b*, 59(3):1758, 1999.

[45] Peter E Blöchl. Projector augmented-wave method. *Physical review B*, 50(24):17953, 1994.

[46] Gopalakrishnan Sai Gautam and Emily A Carter. Evaluating transition metal oxides within dft-scan and scan+u frameworks for solar thermochemical applications. *Physical Review Materials*, 2(9):095401, 2018.

[47] Olivia Y Long, Gopalakrishnan Sai Gautam, and Emily A Carter. Evaluating optimal u for 3 d transition-metal oxides within the scan+u framework. *Physical Review Materials*, 4(4):045401, 2020.

[48] S Swathilakshmi, Reshma Devi, and Gopalakrishnan Sai Gautam. Performance of the r^{2}scan functional in transition metal oxides. *Journal of chemical theory and computation*, 19(13):4202–4215, 2023.

[49] Sergei L Dudarev, Gianluigi A Botton, Sergey Y Savrasov, CJ Humphreys, and Adrian P Sutton. Electron-energy-loss spectra and the structural stability of nickel oxide: An lsda+u study. *Physical Review B*, 57(3):1505, 1998.

[50] Vladimir I Anisimov, Jan Zaanen, and Ole K Andersen. Band theory and mott insulators: Hubbard u instead of stoner i. *Physical Review B*, 44(3):943, 1991.

[51] Jianwei Sun, Adrienn Ruzsinszky, and John P Perdew. Strongly constrained and appropriately normed semilocal density functional. *Physical review letters*, 115(3):036402, 2015.

[52] Hendrik J Monkhorst and James D Pack. Special points for brillouin-zone integrations. *Physical review B*, 13(12):5188, 1976.

[53] J. D. Hunter. Matplotlib: A 2d graphics environment. *Computing in Science & Engineering*, 9(3):90–95, 2007.

[54] Gopalakrishnan Sai Gautam and Pieremanuele Canepa. Theoretical modelling of multivalent ions in inorganic hosts. 2019.

[55] Prasanna V Balachandran, Antoine A Emery, James E Gubernatis, Turab Lookman, Chris Wolverton, and Alex Zunger. Predictions of new abo$_3$ perovskite compounds by combining machine learning and density functional theory. *Physical Review Materials*, 2(4):043802, 2018.

[56] MK Aydinol, AF Kohan, and G Ceder. Ab initio calculation of the intercalation voltage of lithium-transition-metal oxide electrodes for rechargeable batteries. *Journal of power sources*, 68(2):664–668, 1997.

[57] Daniel Sheppard, Rye Terrell, and Graeme Henkelman. Optimization methods for finding minimum energy paths. *The Journal of chemical physics*, 128(13), 2008.

[58] Graeme Henkelman, Gísli Jóhannesson, and Hannes Jónsson. Methods for finding saddle points and minimum energy paths. *Theoretical methods in condensed phase chemistry*, pages 269–302, 2002.

[59] John P Perdew, Kieron Burke, and Matthias Ernzerhof. Generalized gradient approximation made simple. *Physical review letters*, 77(18):3865, 1996.

[60] Reshma Devi, Baltej Singh, Pieremanuele Canepa, and Gopalakrishnan Sai Gautam. Effect of exchange-correlation functionals on the estimation of migration barriers in battery materials. *npj Computational Materials*, 8(1):160, 2022.

[61] Petr Vanysek. Electrochemical series. *CRC handbook of chemistry and physics*, 8:8–33, 2000.

[62] Hatice Aylin Karahan Toprakci and Ozan Toprakci. Recent advances in new-generation electrolytes for sodium-ion batteries. *Energies*, 16(7):3169, 2023.

[63] Feng Wu, Na Zhu, Ying Bai, Libin Liu, Hang Zhou, and Chuan Wu. Highly safe ionic liquid electrolytes for sodium-ion battery: wide electrochemical window and good thermal stability. *ACS applied materials & interfaces*, 8(33):21381–21386, 2016.

[64] Rene Koksbang. Lithium battery electrode compositions, April 30 1996. US Patent 5,512,214.

[65] Daniel C Hannah, Gopalakrishnan Sai Gautam, Pieremanuele Canepa, and Gerbrand Ceder. On the balance of intercalation and conversion reactions in battery cathodes. *Advanced Energy Materials*, 8(20):1800379, 2018.

[66] Rahul Malik, Aziz Abdellahi, and Gerbrand Ceder. A critical review of the li insertion mechanisms in lifepo$_4$ electrodes. *Journal of the electrochemical society*, 160(5):A3179, 2013.

[67] Dereje Bekele Tekliye, Ankit Kumar, Xie Weihang, Thelakkattu Devassy Mercy, Pieremanuele Canepa, and Gopalakrishnan Sai Gautam. Exploration of nasicon frameworks as calcium-ion battery electrodes. *Chemistry of Materials*, 34(22):10133–10143, 2022.

[68] GG Amatucci, JM Tarascon, and LC Klein. Cobalt dissolution in licoo$_2$-based non-aqueous rechargeable batteries. *Solid state ionics*, 83(1-2):167–173, 1996.

[69] Wang Lu, Juefan Wang, Gopalakrishnan Sai Gautam, and Pieremanuele Canepa. Searching ternary oxides and chalcogenides as positive electrodes for calcium batteries. *Chemistry of Materials*, 33(14):5809–5821, 2021.

[70] Kechun Wen, Weiqiang Lv, and Weidong He. Interfacial lattice-strain effects on improving the overall performance of micro-solid oxide fuel cells. *Journal of Materials Chemistry A*, 3(40):20031–20050, 2015.

[71] Cristina Tealdi, Jennifer Heath, and M Saiful Islam. Feeling the strain: enhancing ionic transport in olivine phosphate cathodes for li-and na-ion batteries through strain effects. *Journal of materials chemistry A*, 4(18):6998–7004, 2016.

[72] Mingzhen Jia, Hongyan Wang, Zhandong Sun, Yuanzheng Chen, Chunsheng Guo, and Liyong Gan. Exploring ion migration in li$_2$mnsio$_4$ for li-ion batteries through strain effects. *RSC advances*, 7(42):26089–26096, 2017.

[73] Hanxiao Liao, Lingling Xie, Yan Zhang, Xiaoqing Qiu, Simin Li, Zhaodong Huang, Hongshuai Hou, and Xiaobo Ji. Mo-doped gray anatase tio$_2$: lattice expansion for enhanced sodium storage. *Electrochimica Acta*, 219:227–234, 2016.

[74] Jianguo Sun, Dongxiao Ji, Hualin Ye, Bingxue Yu, Yumei Wang, Seeram Ramakrishna, and Li Lu. Doping induced hierarchical lattice expansion of cobalt diselenide/carbon nanosheet hybrid for fast and stable sodium storage. *Cell Reports Physical Science*, 1(7), 2020.

[75] Siby Thomas, Eun Bi Nam, and Sang Uck Lee. Atomistic dynamics investigation of the thermomechanical properties and li diffusion kinetics in ψ-graphene for lib anode material. *ACS applied materials & interfaces*, 10(42):36240–36248, 2018.

[76] Rashid Khan, Wenjun Yan, Waqar Ahmad, Zhengwei Wan, Shabab Hussain, Akif Zeb, Muhammad Farooq Saleem, Min Ling, and Chengdu Liang. Role of moderate strain engineering in nickel sulfide anode for advanced sodium-ion batteries. *Journal of Alloys and Compounds*, 963:171196, 2023.

[77] Ying Yang, Yuzhang Feng, Zhuo Chen, Yiming Feng, Qun Huang, Cheng Ma, Qingbing Xia, Chaoping Liang, Liangjun Zhou, M Saiful Islam, et al. Strain engineering by atomic lattice locking in p2-type layered oxide cathode for high-voltage sodium-ion batteries. *Nano Energy*, 76:105061, 2020.

[78] Olivia Y Long, Gopalakrishnan Sai Gautam, and Emily A Carter. Assessing cathode property prediction via exchange-correlation functionals with and without long-range dispersion corrections. *Physical Chemistry Chemical Physics*, 23(43):24726–24737, 2021.

[79] Huiwen Ji, Alexander Urban, Daniil A Kitchaev, Deok-Hwang Kwon, Nongnuch Artrith, Colin Ophus, Wenxuan Huang, Zijian Cai, Tan Shi, Jae Chul Kim, et al. Hidden structural and chemical order controls lithium transport in cation-disordered oxides for rechargeable batteries. *Nature communications*, 10(1):592, 2019.

[80] Bin Ouyang, Nongnuch Artrith, Zhengyan Lun, Zinab Jadidi, Daniil A Kitchaev, Huiwen Ji, Alexander Urban, and Gerbrand Ceder. Effect of fluorination on lithium transport and short-range order in disordered-rocksalt-type lithium-ion battery cathodes. *Advanced Energy Materials*, 10(10):1903240, 2020.

[81] Changbao Zhu, Chao Wu, Chia-Chin Chen, Peter Kopold, Peter A van Aken, Joachim Maier, and Yan Yu. A high power–high energy $na_3v_2(po_4)_2f_3$ sodium cathode: investigation of transport parameters, rational design and realization. *Chemistry of Materials*, 29(12):5207–5215, 2017.

[82] Thibault Broux, Tahya Bamine, François Fauth, Laura Simonelli, Wojciech Olszewski, Carlo Marini, Michel Ménétrier, Dany Carlier, Christian Masquelier, and Laurence Croguennec. Strong impact of the oxygen content in $na_3v_2(po_2)_2f_{3-y}o_y$ $0 \leq y < 0.5$ on its structural and electrochemical properties. *Chemistry of Materials*, 28(21):7683–7692, 2016.

[83] Kosuke Kawai, Daisuke Asakura, Shin-ichi Nishimura, and Atsuo Yamada. 4.7 v operation of the cr^{4+}/cr^{3+} redox couple in $na_3cr_2(po_4)_2f_3$. *Chemistry of Materials*, 33(4):1373–1379, 2021.